Growth model for high-Al containing CVD TiAlN coatings on cemented carbides using intermediate layers of TiN

Surface & Coatings Technology 421 (2021) 127361

Contents lists available at ScienceDirect

Surface & Coatings Technology

journal homepage: www.elsevier.com/locate/surfcoat

Growth model for high-Al containing CVD TiAlN coatings on cemented carbides using intermediate layers of TiN

Mohamed Ben Hassine [a], Hans-Olof Andrén [a], Anand H.S. Iyer [a], Antiope Lotsari [b], Olof Bäcke [a], Dirk Stiens [c], Wiebke Janssen [c], Thorsten Manns [c], Johannes Kümmel [c], Mats Halvarsson [a,*]

[a] Dept. of Physics, Chalmers University of Technology, SE-412 96 Gothenburg, Sweden
[b] Dept. of Chemistry and Chemical Engineering, Chalmers University of Technology, SE-412 96 Gothenburg, Sweden
[c] Walter AG, Derendinger Str. 53, DE-72072 Tübingen, Germany

ARTICLE INFO

Keywords:
HRSTEM
Nanolamellae
LP-CVD TiAlN/TiN
Texture
Growth model

ABSTRACT

This work concerns high Al-containing $Ti_xAl_{1-x}N$ coatings prepared using low pressure-chemical vapour deposition (LP-CVD). The coatings were examined using electron microscopy techniques, such as scanning transmission electron microscopy (STEM), energy dispersive X-ray analysis (EDX) and transmission Kikuchi diffraction (TKD). An intermediate TiN-layer with a ⟨211⟩ texture consisting of twinned, needle-shaped grains influences the subsequent growth of the TiAlN layer. The TiAlN grains were columnar with a texture of ⟨211⟩. As the grains grow along ⟨111⟩, with {001} facets, this led to a tilted pyramid surface morphology. The grains developed an internal periodic epitaxial nanolamella structure. The thicknesses were 2 nm for the low (x = 0.6) and 6 nm for the high (x = 0.9) Al-containing lamellae. The TiAlN layer growth could be described by a "two-wing" model, where two TiAlN grains with a twin-related orientation grow on a twinned TiN grain, where the two TiAlN grains gradually switch sides, making the appearance of two wings of columnar grains. In general, this work shows that it should be possible to control the growth of TiAlN layers by controlling the texture and morphology of an intermediate layer, such as TiN.

1. Introduction

Coated tool inserts are widely used in metal cutting applications like turning, milling, parting and grooving. Cemented carbide is often used as substrate material, mainly containing tungsten carbide and a cobalt-rich binder phase [1]. To increase cost efficiency and productivity, as well as process reliability, hard coatings are deposited on the substrates [2]. Metastable $Ti_{1-x}Al_xN$ with a cubic crystal structure is established as an excellent material for cutting tool applications, exhibiting high hardness, high wear resistance and low oxidation rate [3]. It has been reported that an increase of the Al content in $Ti_{1-x}Al_xN$ improves its hardness and high-temperature oxidation resistance [4]. $Ti_{1-x}Al_xN$ prepared using physical vapour deposition (PVD), in which x is below ~0.65, can undergo spinodal decomposition during annealing above ~800 °C, forming coherent cubic-phase c-TiN and c-AlN nano-sized domains. During further thermal treatment above ~1200 °C, c-AlN transforms into stable wurtzite crystal structure w-AlN, which results in coating softening and hardness decay [5].

Cubic $Ti_{1-x}Al_xN$ coatings with high Al content of $x > 0.8$ have been successfully deposited via low-pressure chemical vapour deposition (LP-CVD), by using highly chemically reactive NH_3 gas and the $TiCl_4$–$AlCl_3$–H_2 precursor system at temperatures below 850 °C [6]. These single cubic phase c-$Ti_{1-x}Al_xN$ coatings with a higher aluminium content are receiving increased attention, and considerable efforts have been devoted to address their performance by understanding their microstructure. One key approach is to control the preferred orientation in the coatings. Paseuth et al. produced Al-rich c-$Ti_{1-x}Al_xN$ coatings with controllable preferred crystal orientations using LP-CVD in an industrial plant [7]. They found that the hardness of the c-$Ti_{1-x}Al_xN$ coatings varied from 33 to 36 GPa, depending on whether the preferred orientation was ⟨100⟩ or ⟨111⟩. Furthermore, Ruppi suggested that the life of an α-Al_2O_3 coating with ⟨0001⟩-preferred

* Corresponding author.
E-mail address: mats.halvarsson@chalmers.se (M. Halvarsson).

https://doi.org/10.1016/j.surfcoat.2021.127361
Received 8 November 2020; Received in revised form 22 May 2021; Accepted 24 May 2021
Available online 31 May 2021

orientation was double that of a coating with random orientation during a machining operation [8]. Thus, controlling and understanding the preferred growth orientations in c-$Ti_{1-x}Al_xN$ coatings can facilitate delineation of guidelines for developing high-performance tools.

An interesting feature that has been observed in the CVD c-$Ti_{1-x}Al_xN$ grains is the presence of more or less periodic TiAlN nanolamellae with an alternating Al/Ti ratio [7,9–13]. These formations are believed to be caused by oscillatory surface reactions during deposition and/or spinodal decomposition [7,8]. Recently [14] it was shown that it is possible to tune the nanolamella periodicity by using a rotational gas supply, creating a periodic change in the local deposition conditions. It has also been shown [13] that these nanolamella structures break down at high gas flow rates and the normally columnar TiAlN grain structure disappears.

Wear resistant coatings usually have a multilayer architecture, wherein TiN is the first layer deposited onto the cemented carbide substrate. It exhibits a good adhesion and serves as a nucleation layer for the subsequent layer. This TiN layer cannot inherit any texture from the randomly oriented WC grains in the cemented carbide substrate, but Chen et al. reported that TiN may have different textures, depending on the deposition temperature and nitrogen concentration [15]. It is obvious that the texture of TiN affects its growth, such as grain size and grain shape. Therefore, it is important to understand the microstructure and morphology of the TiN layer in order to enable controlled growth of the following layers, such as $Ti_{1-x}Al_xN$.

Also, the presence of the relatively small mismatch of ~4% between the lattice parameters of c-TiN (a = 4.24 Å) and c-$Ti_{0.2}Al_{0.8}N$ (a = 4.08 Å, calculated by linear interpolation using a = 4.045 Å for cubic AlN [16]) is expected to generate strain at the interface between the two phases in the case of cube-on-cube epitaxy [9,17]. This strain may cause a decrease of the adhesion of the TiAlN layer to the TiN layer that could considerably reduce the wear resistance of the tool. Thus, it is important to investigate factors that may influence the adhesion between different materials used in hard coatings.

TiAlN layers are used on commercial tool inserts and have been found to exhibit enhanced resistance against wear in intermittent cutting, especially during high-speed machining of steels. However, the details of the TiAlN composition, microstructure and residual stress remain unclear, especially when using CVD. It is crucial to understand how the atomic structure changes with the deposition conditions, as well as the mechanisms responsible for nanolamella formation. Also, it is useful to understand the reasons behind different morphologies and how the TiN layer affects the growth (texture) of TiAlN. It should be underlined that the interpretation of electron diffraction patterns and high-resolution transmission electron microscopy (HRTEM) imaging in complex systems formed by light and heavy elements (N; Al; Ti) is a delicate undertaking that should be accompanied by spectroscopic techniques to correlate structural information to elemental chemical analysis. Thanks to recent progress in aberration correction, atomic resolution can nowadays be achieved in 2D using high angle annular dark field scanning transmission electron microscopy (HAADF-STEM) [18,19] enabling structure characterisation at the atomic scale [20,21]. However, one should not forget that these results are only 2D projections of a three-dimensional (3D) object.

In the present work, we use a combination of HAADF-STEM and energy dispersive X-ray spectrometry (EDX) to probe the atomic structure of a wear resistant coating comprising a cubic $Ti_{1-x}Al_xN$ with a specific preferential ⟨211⟩ crystallographic texture, deposited on the top of a TiN layer, which was deposited onto a cemented carbide substrate. The coating was fabricated via LP-CVD in an industrial plant, using an $AlCl_3$–$TiCl_4$–NH_3–Ar–H_2 precursor system. Based on the results of atomic scale structural imaging and chemical microanalysis, the crystal orientation relationship between TiN and TiAlN was identified, together with the influence on the subsequent growth of TiAlN. To our knowledge, this is the first time that the growth mechanism of TiAlN is described in relation to the TiN structure.

2. Materials and methods

2.1. Materials

This study concerns coated cutting tool inserts consisting of a substrate of cemented carbide, mainly containing tungsten carbide and a cobalt-rich binder phase, and a layered wear resistant coating having a thickness of about 5 μm. A TiN layer was deposited onto a polished cemented carbide substrate at a temperature of 850 °C and a pressure of 150 mbar in an industrial scale LP-CVD reactor using $TiCl_4$, N_2, and H_2 reaction gases. Then, a TiAlN layer was deposited immediately on top of TiN without any intermediate layer. The layer of titanium aluminium nitride, $Ti_{1-x}Al_xN$ was deposited at a reaction temperature of 700 °C and a pressure below 20 mbar. The deposition time was 67 min. The precursors were supplied into the CVD reactor by a rotating gas supply (from the centre) with a rotation speed of 5 rpm. The simplified overall deposition reactions for TiN and TiAlN are as follows:

$$\textbf{TiN}: TiCl_4(g) + 0.5\ N_2(g) + 2\ H_2(g) \rightarrow TiN(s) + 4\ HCl(g)$$

$$\textbf{Ti}_{1-x}\textbf{Al}_x\textbf{N}: (1–x)\ TiCl_4(g) + x\ AlCl_3(g) + NH_3(g) + (0.5–0.5x)\ H_2(g) \rightarrow Ti_{1-x}Al_xN(s) + (4–x)\ HCl(g)$$

2.2. Materials analysis

The morphology and cross-sections of the inserts and the general coating appearance, including coating uniformity, were studied using scanning electron microscopy (SEM) in an FEI Versa 3D, which is a combined FIB/SEM system (FIB = Focussed Ion Beam), equipped with a field emission gun (FEG). SEM images were recorded at an accelerating voltage of 2 kV. No coatings were applied to the specimens. To determine the texture X-ray diffraction (XRD) pole figure measurements were done on a XRD3003 PTS X-ray diffractometer of GE Sensing and Inspection Technologies using CuKα-radiation. The X-ray tube was run in point focus at 40 kV and 40 mA. A parallel beam optic using a poly-capillary collimating lens with a pinhole of either 1 or 2 mm diameter as measuring aperture was used on the primary side. On the secondary side a Soller slit with a divergence of 0.4° and a 25 μm thick Ni Kβ filter was used. For the fcc-TiAlN layer{111} pole figures were measured at 2θ angles of 38.266° at tilt angles of $0° \leq \alpha \leq 80°$ in increments of 5° and azimuth angles of $0° \leq \beta \leq 360°$ in increments of 5°. No defocussing correction was applied.

For TEM sample preparation, the FIB/SEM system was used. It is equipped with a liquid gallium ion source and a system for ion- and electron-assisted deposition of Pt. With the aid of this system, cross sections were prepared as thin lamellae from the CVD coating by an in-situ lift-out technique and thinned to sufficient electron transparency (<100 nm).

Electron backscatter diffraction (EBSD) was performed on the sample surface in order to obtain an overview of the grain orientations with respect to the growth direction of the coating. An initial attempt was made to perform EBSD on unprepared sample surfaces that consisted of small pyramids. However, since the surface roughness led to low indexing of the Kikuchi patterns, the sample surfaces were prepared using FIB milling at a low incident angle at a voltage of 15 kV and a current of 500 pA in order to obtain a flat surface and improve the indexing ratio. EBSD was performed using an HKL Channel 5 system and an acceleration voltage of 20 kV and 1.5 nA current over an area of approx. 12 × 8 μm^2 using a step size of 50 nm. Transmission Kikuchi diffraction (TKD) was performed at 30 kV and 30 nm step size on an electron transparent foil of the coating cross section. The EBSD and TKD were performed in a TESCAN GAIA3 FIB-SEM.

TEM and STEM experiments were performed using a Cs-corrected FEI Titan 80–300 TEM/STEM microscope equipped with a FEG source and a monochromator, operated at 300 kV. STEM images were collected by Bright Field (BF) and HAADF detectors. STEM images were acquired with a probe current of ~100 pA and a convergence semi-angle of 20

mrad and processed using the FEI TIA (TEM Imaging & Analysis) software. Compositional analyses were conducted in STEM mode with an Oxford X-ray energy dispersive spectrometer controlled by the TIA software. Typical errors of the measurements are estimated to be ±1 at. %. Image processing was made with the Gatan software DigitalMicrograph. Stereographic projections were calculated using Ideal Microscope software.

3. Results and discussion

3.1. General surface morphology and texture of the TiAlN coating: SEM, EBSD

Fig. 1.a shows an SEM micrograph of the coating surface of the investigated sample. The overview highlights that the morphology of the TiAlN grains consists of "pyramid" grains with a size varying between 500 nm and 1 μm (Fig. 1.a). The pyramids have straight edges and are slightly tilted away from the coating surface normal.

EBSD data were collected from the coating surface in order to identify the TiAlN coating texture. The obtained inverse pole figure (IPF) map is shown in Fig. 1.b and the colour legend is presented in Fig. 1.c. The indexing rate was low due to the surface roughness, but the map shows a clear texture close to {111} (only blue coloured grains). Pole figures and inverse pole figures were plotted using the data obtained in order to determine how much the surface normal direction deviates from {111}. The {111} pole figure shows that most of the grains have {111} oriented at an angle from the surface normal direction (Fig. 1.d). An intensity IPF plot made along the growth direction shows a maximum at the ⟨211⟩ direction, implying that most grains are oriented close to this direction (Fig. 1.e). Even though the statistics is limited, the data clearly indicate a ⟨211⟩ fibre texture parallel to the surface normal. The angle between the ⟨111⟩ and ⟨211⟩ directions is 19.5°. The coating phase content was checked by X-ray diffraction (XRD). It was found that cubic TiAlN was the main phase with only minor h-AlN being present (not shown). An XRD {111} pole figure is shown in Fig. 1.f together with a cross section of the intensity distribution in Fig. 1.g. The X-ray data confirm the conclusions drawn from the EBSD analysis; the coating has a ⟨211⟩ texture (along the surface normal) with {111} plane normals at an angle with respect to the coating normal.

3.2. General morphology and texture of the TiAlN cross section: SEM, FIB, TKD

TKD data was collected from the FIB lamella in order to get information about the crystallographic texture in the coating cross section. The obtained band contrast reveals a columnar morphology of the TiAlN

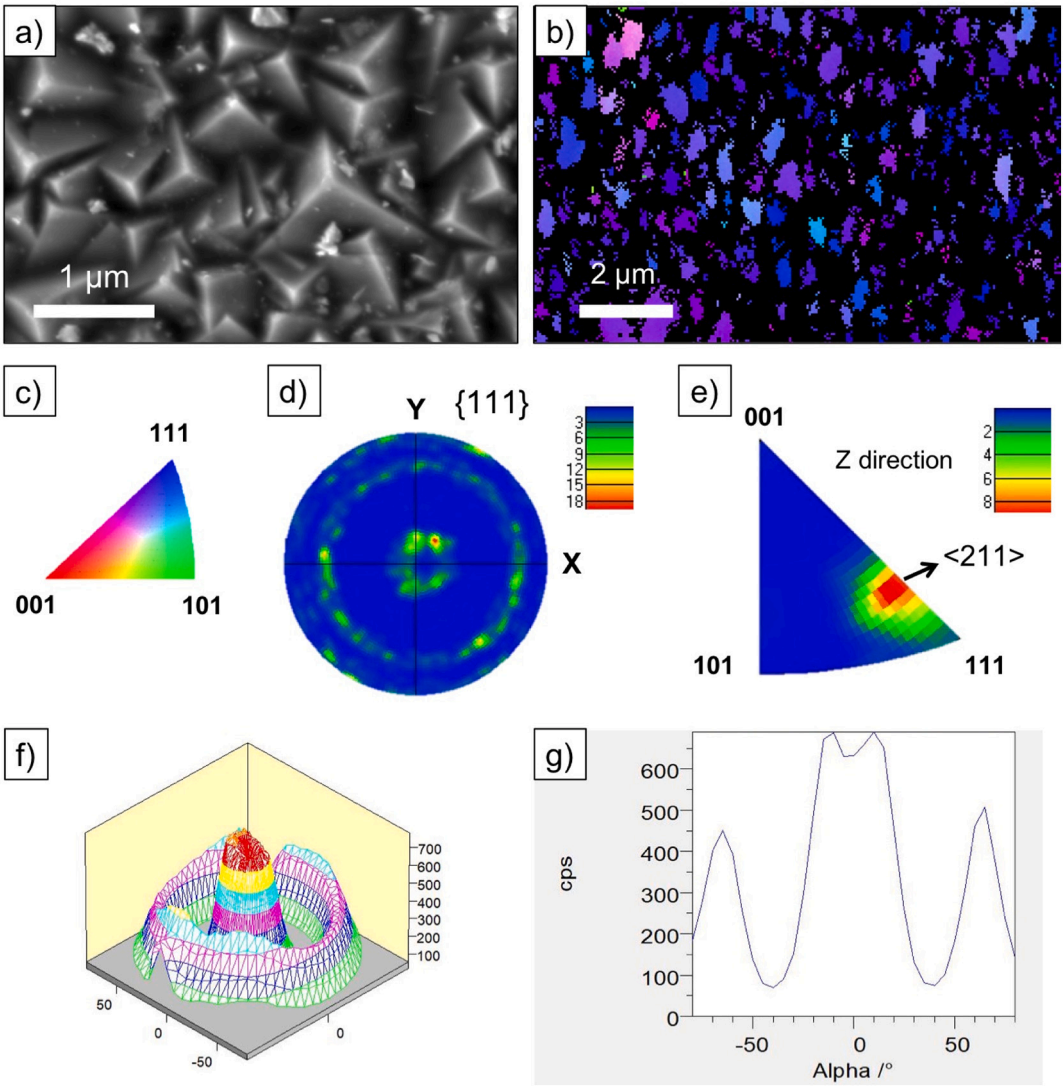

Fig. 1. a) SEM micrograph collected from the coating surface highlights a pyramid morphology for the TiAlN grains; b) EBSD inverse pole figure (IPF) map along the coating normal; c) colour legend for the IPF map in b); d) {111} pole figure contour plot; e) IPF intensity plot along the coating normal; f) XRD {111} pole figure; g) intensity plot across the centre of the pole figure in f.

coating, in which the grains are slightly tilted versus the coating normal (Fig. 2.a). The TiN coating has a fine-grained structure with a grain size of about 100 nm, whereas TiAlN shows a distinct columnar growth with grain widths of around 0.5 μm and heights of several microns; often the grains extend almost all the way through the layer. The obtained IPF map is shown in Fig. 2.b and the colour legend in Fig. 2.c. The indexing rate was lower at the bottom part of the coating as the grain size was smaller there. In addition, there is an unintentional hole in the sample due to specimen preparation (ion milling), but the map still shows a clear texture close to the ⟨111⟩ direction (mostly blue grains). An IPF intensity plot along the surface normal direction shows a peak at the ⟨211⟩ direction, indicating that most grains are oriented close to this direction (Fig. 2.d). Thus, the TKD data confirms the fibre texture obtained from the XRD data and the SEM/EBSD measurements on the surface, and also shows that the texture extends throughout the whole coating, at least for grains large enough to be indexed.

The TiAlN microstructure was further examined by various TEM techniques in order to better understand the formation of the tilted pyramid morphologies. Several areas were analysed in order to get good microstructural statistics. The data from the various grains were very similar, and typical data are shown in the next section.

3.3. General view of FIB cross section: TEM

Fig. 3 shows a cross-sectional BF-STEM micrograph of the coating providing an overview of the TiAlN and TiN microstructures, in both cases consisting of columnar grains. The thicknesses for TiN and TiAlN are about 1.2 μm and 4.1 μm, respectively. Single bright and dark grains are due to different grain orientations and thereby changing diffracting conditions. For the TEM characterisation two TiAlN grains were selected, marked by the blue and yellow arrows in Fig. 3. Both start growing as rather narrow grains with an increasing width with increased coating thickness. The two grains start to grow at the TiN/TiAlN interface and continue to the coating surface. The first grain is slightly inclined with respect to the coating normal and has a V-shaped morphology (arrow number 1 in Fig. 3). The second grain (arrow number 2 in Fig. 3) grows rather parallel with the coating normal (at least as viewed in the micrograph; it could be tilted in a perpendicular direction, out from the thin foil), and it has a kind of zig-zag morphology. For the interface between

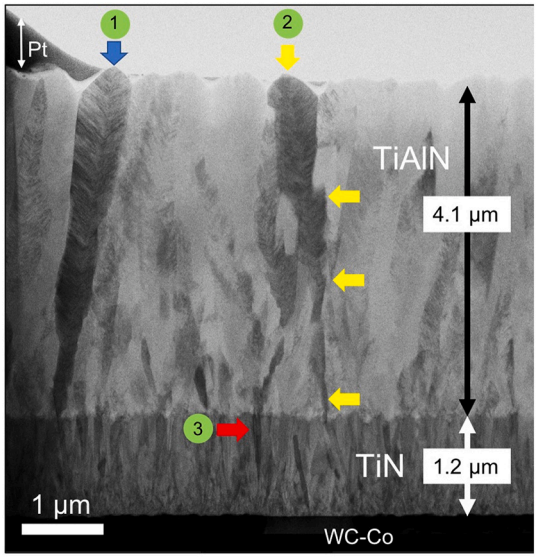

Fig. 3. BF-STEM image of the cross-section FIB lift-out lamella. The numbers indicate the investigated grains of TiAlN and TiN in this work. Number 1 and 2 correspond to an inclined and a zigzag TiAlN grain, respectively. Number 3 corresponds to a TiN grain at the TiN/TiAlN interface.

TiN and TiAlN, we investigate the grain marked by the red arrow number 3 (Fig. 3) further below.

3.4. Tilted grain

3.4.1. Microstructure and texture of TiAlN

Fig. 4.a–c shows HAADF-STEM images collected from the top pyramidal grain 1 of Fig. 3. A periodic alternation of bright and dark lamellae is observed in all TiAlN grains, with thicknesses of approximately 6 nm for dark lamellae and 2 nm for bright lamellae. The interpretation of HRSTEM (high-resolution STEM) HAADF images is generally straightforward because the intensity depends on the average atomic number Z of each atomic column as ~ Z^x, with x typically being slightly lower than 2 [22,23]. Therefore, *Z*-contrast imaging allows direct interpretation of

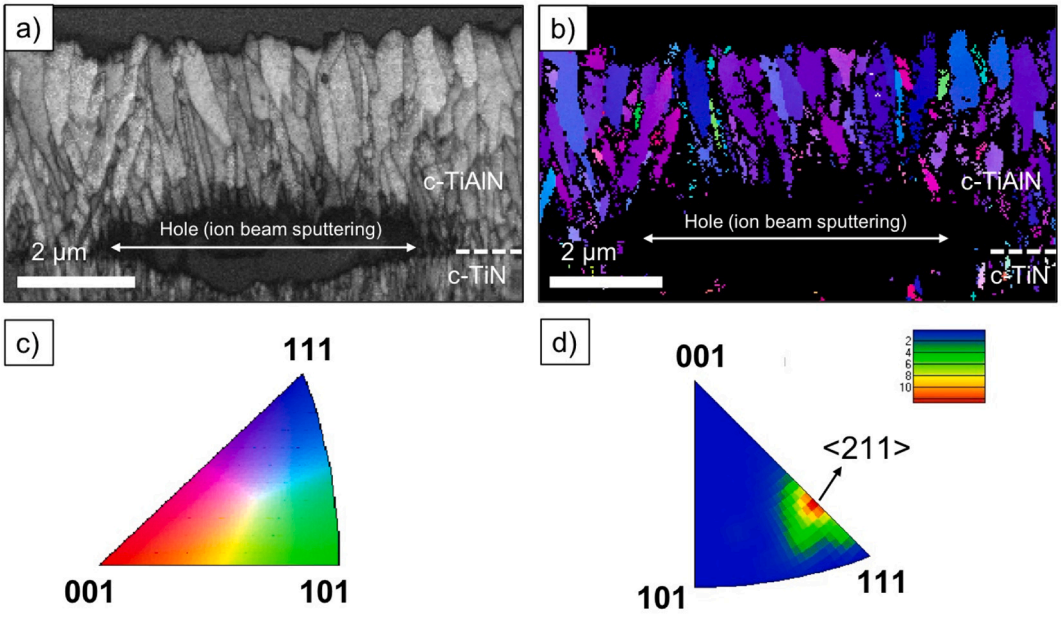

Fig. 2. a) Band contrast TKD image of the cross section showing the columnar morphology of the TiAlN grains. b) IPF map along the coating direction. c) Colour legend for the IPF map in b). d) IPF intensity plot of the TKD data along the surface normal.

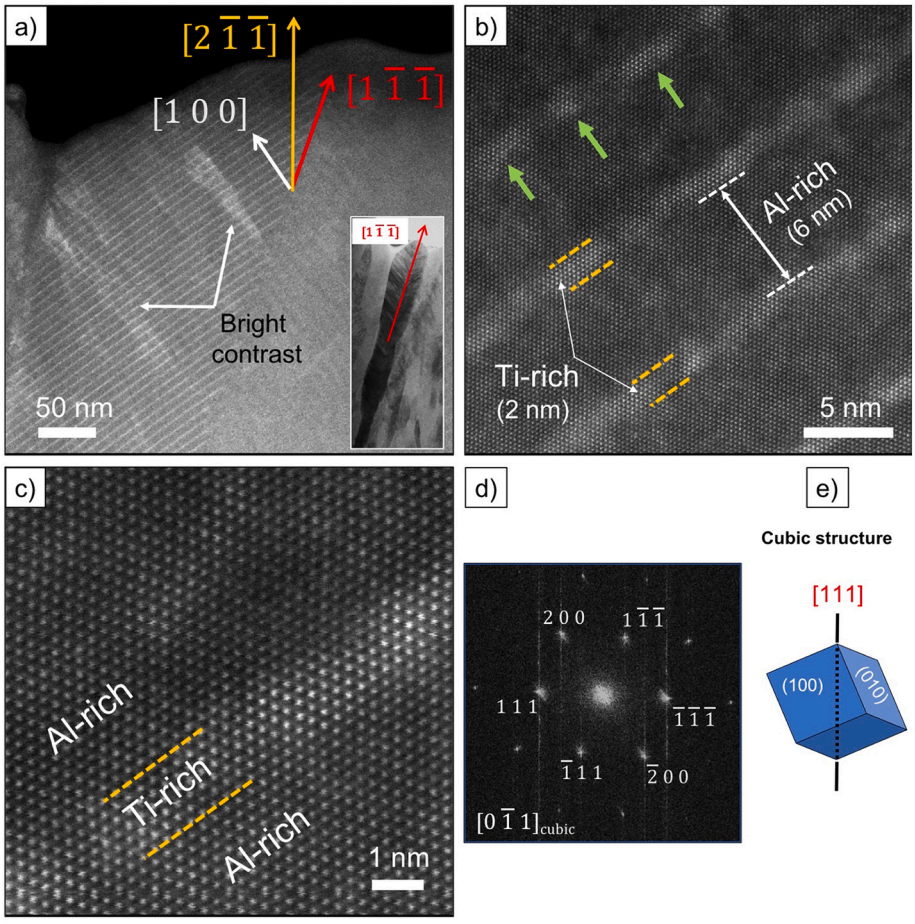

Fig. 4. a–c) HAADF-STEM images of the TiAlN microstructure formed by alternation of Ti-rich and Al-rich lamellae (camera length 195 mm). d) FFT calculated from the HAADF-HRSTEM micrograph of Fig. 4.b. e) A schematic drawing of the cubic geometry highlighting the pyramidal shape of the three {100} faces when the cube is oriented along [111].

atomic structure changes. Ti and Al atomic columns appear significantly brighter in HAADF imaging than N columns, which are generally not heavy enough to produce sufficient intensity, and are therefore not visible. Consequently, the difference in contrast of Fig. 4.b and c represents the difference in the atomic number of Ti and Al. Since Ti has a higher Z than Al, it is obvious that bright lamellae are richer in Ti. In addition, the presence of an inhomogeneity within the bright Ti-rich lamellae can be noted. These do not have a constant brightness, but contain darker and brighter parts (green arrows in Fig. 4.b), probably due to the lamellae not being perfectly straight and homogeneous, but varying slightly in thickness (on the atomic scale).

Fig. 4.d shows a fast Fourier transform (FFT) calculated from the HAADF-HRSTEM micrographs, illustrating that both phases (Ti-rich and Al-rich) exhibit an FCC (face-centred cubic) structure ($Fm\bar{3}m$; a = 4.08 Å [9]). The vertical streaks in the FFT are artefacts produced by the software. Since a coherent lamella microstructure was observed, the presence of an epitaxial relationship between both FCC lamellae is evident. Moreover, the HRSTEM image of Fig. 4.c shows the epitaxy between both lamellae. From the FFT we can conclude that the coating normal is along ⟨211⟩, while the TiAlN grain actually grows along a ⟨111⟩ direction, but this is slightly inclined relative to the coating normal. The grain starts at the underlying TiN layer and extends to the top surface of the coating. It is obvious that the formation of the pyramid surface morphology, having three-fold symmetry, is associated with the growth direction along ⟨111⟩, as was recently reported [13,14] Fig. 4.e is a drawing of a cube oriented along a ⟨111⟩ direction showing the corresponding pyramid morphology (the three {100} faces). In the TiAlN pyramid geometry, the Ti/Al rich lamellae are parallel to the pyramid faces, as they are parallel to {100}, see Fig. 4.

3.4.2. *Chemical analysis*

In order to get better insight into the chemical composition of the material, quantitative energy dispersive X-ray spectroscopy (EDX) was performed of both Al-rich and Ti-rich lamellae. Representative results are shown in Fig. 5.a. Due to the very close energy for the N(K) and Ti(L) peaks, it is very challenging to simultaneously quantify the content of Ti and N. Therefore, only the variation of Ti and Al is taken into account for the quantification, and no attempt to measure the N content is made. Quantitative point EDX analysis gives a composition of about $Ti_{0.30}Al_{0.70}N$ and $Ti_{0.10}Al_{0.90}N$ (N not measured) for Ti-rich and Al-rich lamellae, respectively. The very good spatial resolution that makes it possible to measure the composition of a 2 nm wide lamella can be explained by the very small probe diameter in the Cs-corrected microscope together with a small average atomic number of the material. Using the single scattering model by Goldstein et al., the beam diameter at the bottom of a 50 nm thick foil was calculated to be only 1.2 nm [24]. Typical spectra from the two types of lamella are shown in Fig. 5. Moreover, EDX linescans were acquired across Ti- and Al-rich lamellae (Fig. 5.b). The compositions are $Ti_{0.38}Al_{0.62}N$ and $Ti_{0.10}Al_{0.90}N$ for Ti-rich and Al-rich lamellae, respectively, and the average material composition is calculated to be $Ti_{0.15}Al_{0.85}N$. These results are in line with [14].

3.4.3. Strain in the TiAlN lattice

Fig. 4.a shows a few bright columnar areas inside a TiAlN grain, perpendicular to the periodic lamellae. Since the HAADF detector gives chemical contrast ($\sim Z^2$), one might think that these bright areas are rich in Ti. However, as shown in the HAADF images in Fig. 6.a–c, the bright contrast can at least partly be attributed to electron diffraction, due to a distortion of atomic columns, probably caused by local strain. For crystals in zone-axis orientations, electron channelling plays an important role in the formation of *Z*-contrast HAADF-STEM images, as the incident electron beam is focused along the atomic columns. Within a distorted lattice, e.g. caused by the presence of dislocations, the displacement of atoms varies along the columns, thereby causing electron dechanneling. The dechanneling reduces or enhances HAADF intensities, depending on the inner collection angle of the detector, giving so-called strain/diffraction contrast [25]. Therefore, by varying the camera length of the TEM, the chemical contrast can be distinguished from the contrast caused by other effects, such as strain and possible ion milling induced thickness variations.

Fig. 6.a–c shows HAADF-STEM images of a TiAlN grain, collected with different camera lengths (CLs); 195 mm, 130 mm, and 77 mm, respectively. These CLs correspond to different scattering angles accepted by the HAADF detector. For 195 mm the range is 39–200 mrad, for 130 mm it is 58–200 mrad and for 77 mm it is 99–200 mrad. Thus, the minimum scattering angle that is detected is largest for CL = 77 mm, giving less diffraction contrast using this setting. For a CL of 195 mm or 130 mm, the HAADF-STEM images consist of bright and dark columnar areas. Reducing the CL to 77 mm, the strain contrast is minimized (Fig. 6.c). Indeed, all the dark and bright columnar areas disappeared (differently strained); only the chemical contrast obtained by Ti-rich and Al-rich lamellae is still observed in this image. Moreover, the HAADF-HRSTEM image (Fig. 6.d) clearly reveals the atom columns in the bright area (Fig. 6.d; region A). However, in the dark area, the atomic resolution is less pronounced, individual points (atom columns) changing to lines (Fig. 6.d; region B), as the atomic columns are slightly tilted compared to region A and consequently the lattice is slightly distorted in this area. Since the main purpose of this article is to understand the growth mechanisms of TiAlN on top of TiN, all the HAADF-STEM images presented below were collected using CL = 195 mm to get some diffraction contrast in order to better visualise local strain and other effects.

An FFT pattern acquired from the TiAlN region in Fig. 6.d is presented in Fig. 6.e, where it can be seen that the lamella normals are oriented along [100]. A closer examination of the FFT reveals the presence of several extra reflections along the [100] direction, see Fig. 6.e. The origin of these extra spots can be explained by the presence of the ordered nano-lamellae in the [100] direction. The FFT was processed by masking the normal diffraction spots (i.e. using only the extra reflections) followed by an inverse FFT. A representative result is shown in Fig. 6.f, where it can be seen that these extra reflections (super-reflections) correspond to the periodic Ti-rich lamellae and to some Ti-rich nanodomains dispersed inside the Al-rich lamellae, as shown by the bright areas. Moreover, the distance between the super-reflections was found to be around 40 times smaller than the distance between (000) and (200), which is in agreement with the ratio of the periodicity of Ti-rich lamellae to the interplanar distance a/2 of (200) planes. The periodicity of Ti-rich lamellae and interplanar distance are approximately 8 nm and 2 Å, respectively.

3.5. Growth mechanism of TiAlN on TiN

In our study, TiN is the first layer deposited on the substrate and it serves as a nucleation layer for the TiAlN layer. As such, it is important to understand the microstructure and morphology of this layer in order to enable controlled growth of the following layer. It has been reported that the preferred orientation and morphology of the TiN layer are related to the deposition temperature and gas concentration. Lower deposition temperatures (~900–1100 °C) favour the formation of twinned crystals and results in ⟨211⟩ textured layers, whereas higher deposition temperature (≥1200 °C) favours twin-free crystals and results in ⟨100⟩ textured layers [15,26]. Different orientations and microstructure of the TiN grains should affect the orientation and other details of the deposited TiAlN layer on top. We carefully examined this interface, its microstructure and chemistry, in order to understand the orientation relationship between both layers and consequently to identify which factors that affect the growth of TiAlN on top of TiN.

Fig. 7.a shows a HAADF-STEM image of the interface between TiN and TiAlN. The overview reveals a needle-like morphology of the TiN grains with twins located vertically, at the middle of the grains, extending to the needle tip. On top of the TiN layer TiAlN starts to grow with small grains, having widths of around 50 nm or smaller. The number of grains that nucleate at the bottom of the TiAlN layer is estimated to be more than 100 times higher than the number of grains present in the top part of the coating. The small grain sizes at the TiN/TiAlN interface make overlap of crystallites possible in the TEM foil and sometimes makes the interpretation of the STEM images difficult, as these images are the projection of a 3D volume onto a 2D plane.

In the HAADF-STEM image presented in Fig. 7.a, TiAlN grows on top of one TiN twinned grain (the twin plane is arrowed). A HAADF-HRSTEM image collected from the middle of the TiAlN area is shown in Fig. 7.b. At the right side of this micrograph, the FFT from area B′ is indexed as an FCC structure. The FFT obtained from the left side, marked by B″, consists of a superposition of two FCC patterns. These two crystalline domains are twin-related by a rotation along [111], see more details below. Some extra reflections (arrowed in Fig. 7.b) are also observed in the FFT from area B″. These reflections are obtained by double diffraction. Higher magnification HAADF-HRSTEM micrographs of areas B′ and B″ are shown as C′ and C″ in Fig. 7.c., respectively. The HRSTEM image of area C′ shows a very ordered stacking of the atomic columns, however, in area C″ the columns are not as well defined, due to an overlap of two TiAlN domains in this region.

In order to further investigate the growth of these two TiAlN domains, we carefully polished the FIB lamella using a low-voltage ion beam to make it even thinner and reduce the domain overlaps. In Fig. 7.d, the two TiAlN domains are labelled and shown in lower magnification. The two domains are actually two grains: the two TiAlN grains, number 1 and 2, grow from the left and right sides (side 1 and 2) of the above-described twinned TiN grain, respectively. The TiAlN grain number 1 grows inclined towards the left and starts from side 1 of the TiN grain (the left twin), then continues to grow to the right with an inclination angle of about 15° relative to the coating normal.

In a similar way, grain number 2 grows inclined towards the right and starts from side number 2 (the right TiN twin) and then later continues to grow to the left. After ion polishing, as the sample became thinner, parts of TiAlN grain 2 were removed and only remained as a small crystallite at the top of TiN side 2 and further up in the TiAlN layer. The lamellae in these two remaining regions of grain 2 are parallel, and are indicated by arrows in Fig. 7.d. These two TiAlN grains are twin-related, due to their origin from the two sides of the twinned TiN grain; see more discussion below.

The HAADF-STEM image in Fig. 7.e. reveals the presence of small nanograins of TiAlN that fill the volume between the needles of the TiN grains. In these small grains the Ti-rich/Al-rich lamellae structure is absent. These grains probably only grow for a limited distance, as they are hindered by the fast-growing TiAlN grains (along ⟨100⟩ directions) that nucleated slightly higher up, on the twinned TiN grains. As the small grains without lamellae grow in the valleys between the TiN needle-shaped grains they might also be slow-growing due to a limited ability for the precursors to access this area during deposition.

The microstructure of the TiAlN material located between side 1 of TiN and TiAlN grain 1, which does not contain a periodic lamellae structure, was checked by HAADF-HRSTEM imaging (Fig. 7.f). The insets in Fig. 7.f show the FFTs from the interfacial region of TiAlN and the left twin of TiN. The two phases exhibit FFT patterns that are identical (except the distances between the reflections are different due to a

difference in lattice parameter), which means that TiAlN grows epitaxially on side 1 of the left TiN twin. Similarly, an FFT calculated from HAADF-HRSTEM image of TiAlN grain number 1 containing a periodic structure has the same FFT pattern as the non-periodic part at the interfacial region (Fig. 7.g). In conclusion, TiAlN grain 1 grows epitaxially on TiN side 1. After some distance the TiAlN growth is more ordered, and the TiAlN grain continues to grow upwards, to the left, forming Ti-rich and Al-rich lamellae. As the TiAlN growth direction is along ⟨111⟩ and since the grain is slightly tilted, the direction being parallel with the coating normal becomes ⟨211⟩. Thus, this explains how grains growing locally along ⟨111⟩ can form a coating with a ⟨211⟩ texture.

3.6. TiN structure

As the substrate was polished before CVD, the TiN grains probably initially have a random orientation, gradually developing the observed 211 texture. The TiN layer contains grains with a slight V shape, as can be seen in Fig. 3. Fig. 9.a presents a HAADF-STEM overview of the top part of the TiN layer, consisting of twinned needle-shaped (or possibly wedge-shaped) grains. Several dislocations are present inside the TiN grain, seen as white lines, starting close to the twin plane and spreading to both sides of the TiN grain. A detailed study of dislocations present in this coating would require a detailed structural analysis of the atomic plane displacements, which is beyond the scope of this work.

Fig. 9.b represents a filtered HAADF-HRSTEM image obtained by applying an inverse FFT from a masked FFT of the twinned TiN area. The insets in Fig. 9.b show FFTs from both sides of the twin, demonstrating the TiN cubic lattice structure ($Fm\bar{3}m$; a = 4.24 Å), with a (111) twin plane. XRD pole figures were acquired in order to further confirm a preferred orientation of the TiN grains, see Fig. 9.c. The intensity maxima in the {111} and {220} pole figures are at α-angles consistent with a ⟨211⟩ texture. The poor signal to noise in all pole figures is due to the layer architecture and low thickness of the TiN layer. The deviation from rotational symmetry in the {220} and {111} pole figures should not be misinterpreted as orientations deviating from a fibre texture. It is due to issues of measurement and sample geometry: in order to get sufficient counting statistics, a relatively large measuring aperture of 2 mm diameter was chosen, causing the irradiating beam to exceed the sample surface (flank side of the cutting insert) at β-angles approaching 0° and 180°, respectively, at low θ-angles. As the XRD {422} pole figure exhibits a centred intensity, this corresponds to a TiN ⟨211⟩ texture (along the coating normal), as expected.

3.7. Chemical composition at the interface TiN - TiAlN

STEM/EDX analysis was carried out to identify the chemical composition in the TiN/TiAlN interfacial region. Fig. 10.b 1′–4′ show EDX spectra collected from points 1–4, respectively, in Fig. 10.a. A comparison of spectra 1′ and 2′ reveals a drastic decrease in the intensity of the Ti-K peak, while the intensity of the N-K/Ti-L peak (around the energy 0.4 keV) is still the same (Fig. 10.b). This means that this peak corresponds mostly to the N-K signal. Therefore, the interfacial layer could be identified as a phase rich in Al and N. The quantification of EDX spectrum 2′ gives a composition of $Ti_{0.04}Al_{0.96}N$ (N not quantified). Moreover, the FFT calculated from the HRSTEM image of this region indicates a cubic structure (Fig. 7.f). Consequently, this area is considered to consist of c-$Ti_{0.04}Al_{0.96}N$ grains.

EDX spectrum 3′ was collected from the interface between the TiN needle top and TiAlN, and it reveals a significant signal of Cl (Fig. 10.b). The quantification of this spectrum indicates the presence of 9 at.% Cl of the total amount, excluding N. Assuming that Cl substitutes N, and assuming a stoichiometric composition with respect to anions, this corresponds to a composition $(Ti_{0.23}Al_{0.77})(N_{0.90}Cl_{0.10})$. At the bottom interface, at point number 4 in Fig. 10.b, only 3.6 at.% Cl of the total amount (excluding N) was detected.

4. Discussion

We have shown in this work that it is possible to deposit a bilayer coating of TiAlN and TiN on cemented carbide substrates using CVD (Figs. 2 and 3). The TiAlN layer had a clear ⟨211⟩ texture all through the thickness of the layer (Figs. 1 and 2). It consisted of columnar grains, many extending from the layer bottom to its top, with a ⟨111⟩ direction along the grain column. The grain width increased from around 50 nm at the bottom to between 500 nm and 1 μm at the top. Three {100} surfaces of each grain formed a pyramid surface morphology, their ⟨111⟩ axes slightly tilted (20°) relative to the surface normal (Figs. 1–3). It is believed that the TiAlN grains grew simultaneously on the three {100} facets, leading to a grain growth along the ⟨111⟩ direction. As the ⟨111⟩ axes of the grains are tilted, this leads to the ⟨211⟩ fibre texture of the coating.

The TiAlN grains had a cubic crystal structure and were built up by nanolamellae along {100} (the three growing facets), consisting of Al-rich layers approximately 6 nm thick, and Al-poorer layers approximately 2 nm thick (Fig. 4). Their composition was approximately $Ti_{0.1}Al_{0.9}N$ and $Ti_{0.4}Al_{0.6}N$, respectively (Fig. 5). This gives an average ratio of Ti/Al = 15/85. The lamellae are probably not atomically smooth with a constant composition, and locally higher values of Ti, both in the Ti-rich and Al-rich lamellae are expected (Fig. 6). The formation of a lamella structure has been proposed to be due to spinodal decomposition [7], but also to oscillating periodic surface reactions during growth [9,10,12]. In addition [14], it was shown that the periodic lamella formation can be controlled by having a rotation gas supply. By varying the rotation speed relative to the coating growth rate the lamella periodicity can be tuned. Basically, each gas supply rotation cycle gives rise to one nanolamella period. In our work a deposition time of 67 min produced a TiAlN layer of 4.1 μm, giving a growth rate of 0.06 μm/min. Using this value and a rotation speed of 5 rpm, Eq. (2) in [14] predicts a periodicity of 7.4 nm, which is very close to the 8 nm (2 + 6 nm), or rather 7.5 nm, see Fig. 4.a, observed here. Thus, the present work confirms the model proposed for lamella formation in [14].

It has been estimated by density functional theory (DFT) simulations that {001} planes of TiAlN have a much lower surface energy than the {111} and {110} planes [27]. This would stabilize the {001} facets during growth, making lamella formation in the ⟨001⟩ growth direction possible. In addition, it was found that the higher the Al concentration the stronger the segregation of Ti towards the surface. Thus, when an Al-rich lamella grows, Ti can be pushed out towards the surface, keeping the Al-concentration high. After some time, these Ti-atoms can be incorporated in a Ti-rich lamella, which leads to subsequent growth of an Al-rich lamella, and the process can be repeated periodically. This is supported by the rotational gas supply, periodically favoring high and low Ti-concentrations in the lamellae, see ref. [14] for details.

Still, the formation of lamellae with the same crystal structure, but distinctly different compositions needs more investigations in order to obtain a deeper understanding of the underlying growth mechanisms.

At the bottom of the TiAlN layer, below the regular nanolamellar TiAlN grains, an interfacial region consisting of smaller nanosized grains existed (Fig. 10). These were found to be cubic TiAlN with a composition of approximately $Ti_{0.04}Al_{0.96}N$, thus being very close to be a cubic AlN phase. These grains did not exhibit a nanolamellar structure. They grew epitaxially onto TiN, and the lamellar TiAlN grains then grew epitaxially on these “AlN” grains. At the interface between TiAlN and TiN some Cl was detected, and the composition in the TiAlN layer close to the tip of a TiN needle was found to be $(Ti_{0.23}Al_{0.77})(N_{0.90}Cl_{0.10})$, assuming stoichiometry with respect to the anions. The Cl is expected to come from titanium and aluminium chlorides in the gas phase.

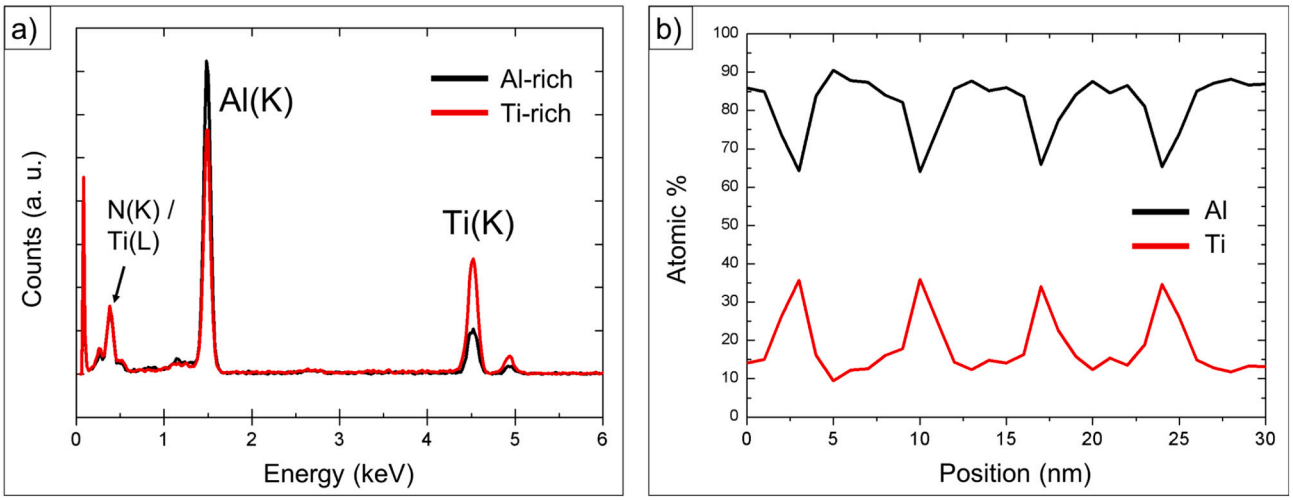

Fig. 5. a) EDX spectra collected from an Al-rich and Ti-rich lamella. These correspond to 90/10 and 70/30 Al/Ti ratios. b) EDX linescans across Ti- and Al-rich lamellae.

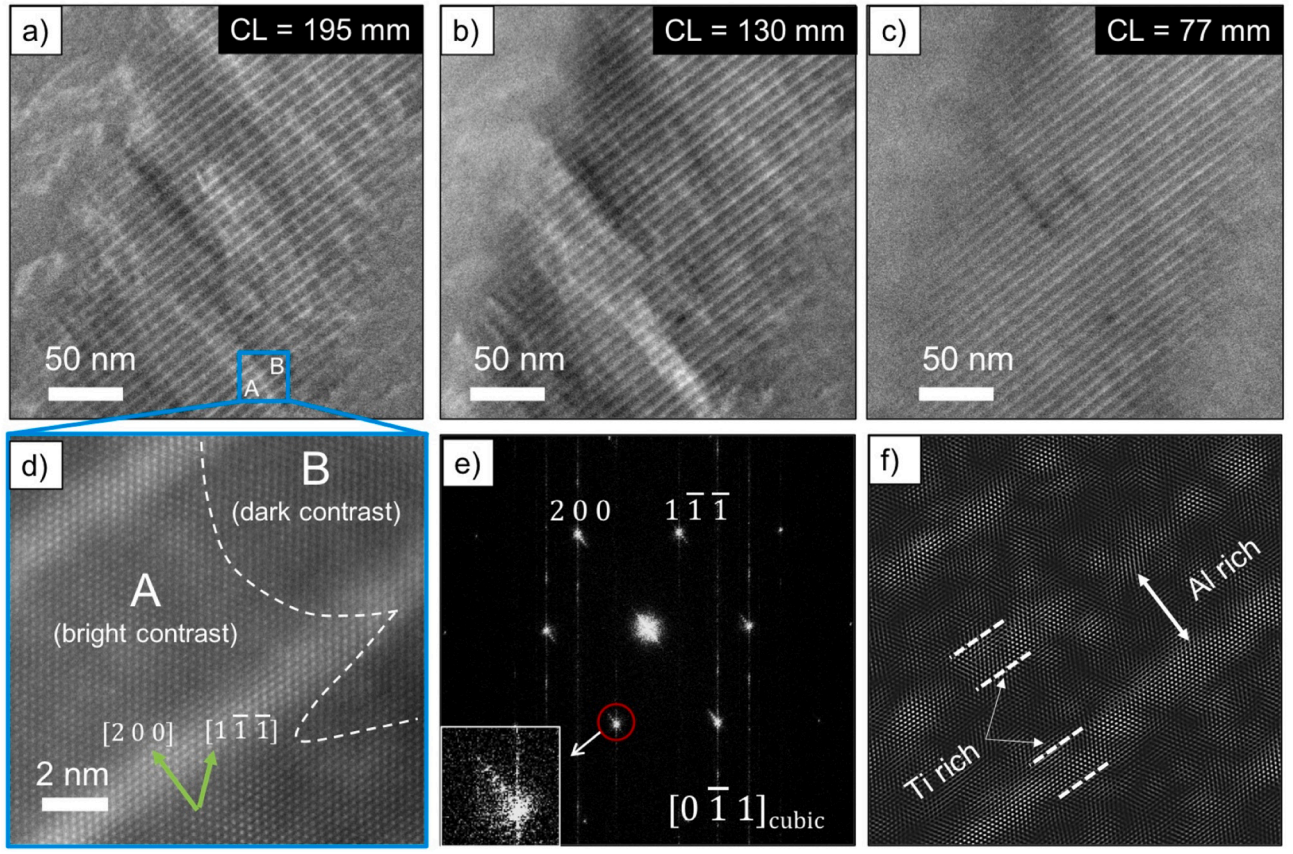

Fig. 6. HAADF-STEM images of TiAlN collected using different TEM camera lengths: a) 195 mm, b) 130 mm, and c) 77 mm. d) HAADF-HRSTEM micrograph showing the atomic resolution of the bright (A) and dark (B) contrast areas, boxed area in (a). e) FFT calculated from a HAADF-HRSTEM image containing both types of TiAlN lamellae (high and low Al/Ti ratio). The FFT exhibits extra reflections in the [100] direction, see the small inset figure. f) Inverse FFT image obtained by using only these extra reflections in e).

The TiN layer was highly columnar and had a grain size of about 100 nm (Fig. 3). The upper part of the TiN layer (Figs. 7–9) consisted of needles (or possibly ridges) with a ⟨211⟩ growth direction (Figs. 7 and 9), containing a {111} twin boundary along the grain centres and some dislocations spreading from this boundary (Fig. 9).

Fig. 11 shows schematic drawings of the growth mechanism, the so-called "two-wings" model, of two TiAlN grains growing on top of a twinned TiN grain. TiAlN grains number 1 and 2 grow from the left and right twin domains, side 1 and 2 respectively, of the TiN grain, see Fig. 11.a. The two TiAlN grains grow epitaxially, with a cube-on-cube relationship to the underlying grains, making the two TiAlN grains twin-related. Initially the TiAlN grains grow without an internal lamella structure with a very high Al content, around 96 at.% (cations). Gradually, after some tenths of nanometres, the TiAlN

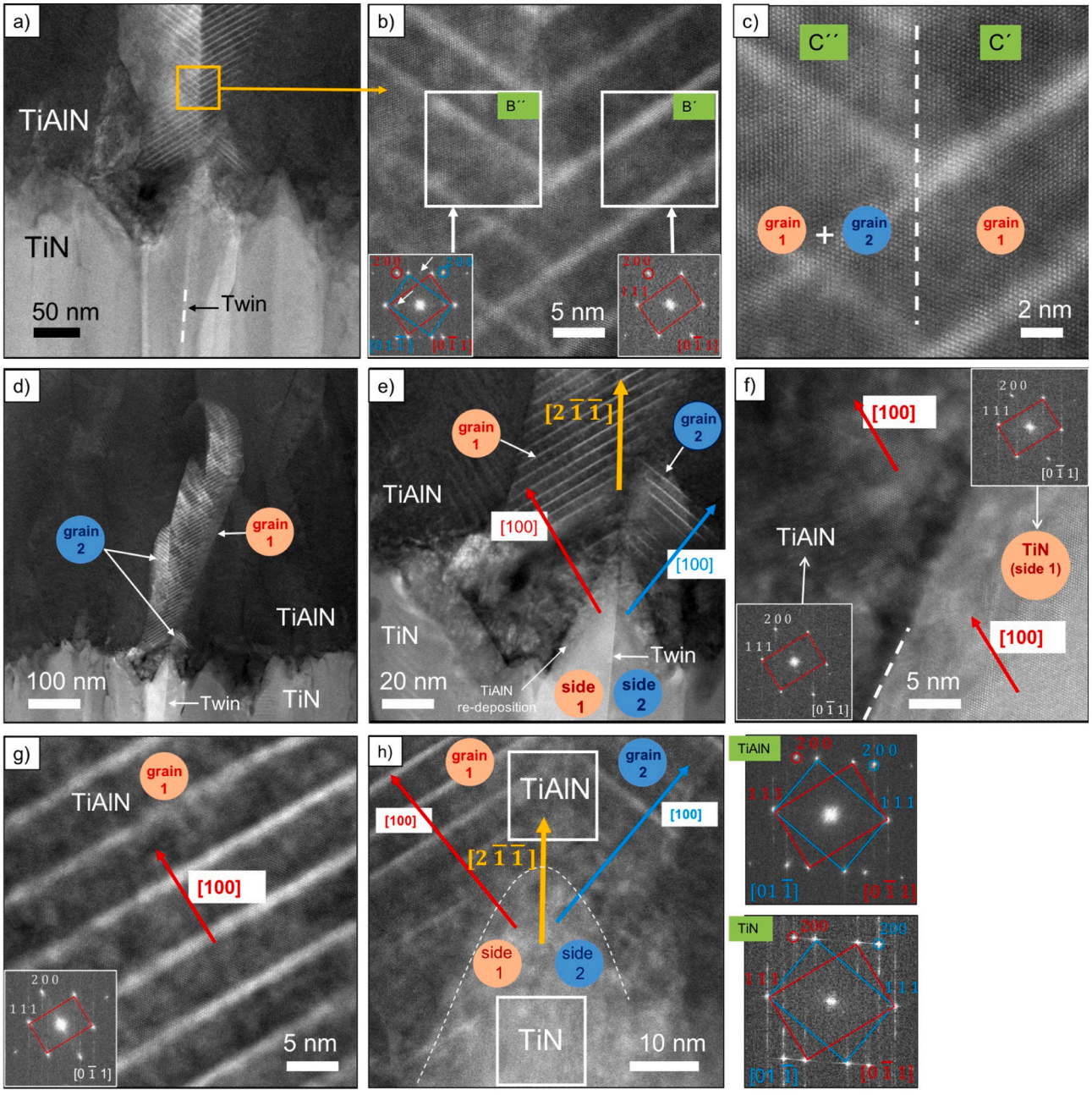

Fig. 7. Interface between TiN and TiAlN; a–e) HAADF-STEM images highlighting the growth of two grains of TiAlN on top of a one twinned grain of TiN. e) HAADF-STEM image shows the presence of an interfacial non-lamella TiAlN structure between the TiN and lamella-TiAlN grains. f–g) HAADF-HRSTEM images demonstrating an epitaxial growth of TiAlN grain number 1 on TiN side 1. h) HAADF-HRSTEM image showing epitaxy between the two grains of TiAlN and the twinned TiN grain. The composite FFTs for the TiAlN grains and the TiN domains are shown as insets.

growth is more "controlled", and the periodic lamella formation starts and generally proceeds throughout the coating. The lamellae grow epitaxially on each other and the underlying "AlN", keeping the (cube-on-cube) relationship with underlying TiN domain.

As also has been described earlier, the TiAlN grains grow preferentially along ⟨111⟩. This makes the left TiAlN grain (1) growing fast to the right, while the other TiAlN grain (2) grows fast to the left. This causes the two TiAlN grains to gradually switch sides, so that grain 1 is to the right (above TiN side 2) and grain 2 is to the left (above TiN side 1), after some hundreds of nanometres. In this way the two grains grow at an angle with respect to each other, forming two "wings", hence the name "two-wing" growth model for the TiAlN coating.

The "two-wing" mechanism can be understood by using stereographic projection. Fig. 12 shows two standard projections along $[2\bar{1}\bar{1}]$, which represents the texture (and coating normal) of the TiAlN coating. Grain 1 and 2 are twin related, as described above, by a (111) mirror plane normal to the coating normal direction, giving the two projections shown in Fig. 12. Thus, these represent the two TiAlN grains viewed from the top. Grain 1 is growing with lamella normals along [100], after the initial stage without lamellae. As can be seen in Fig. 12, the ⟨111⟩ direction closest to $[2\bar{1}\bar{1}]$ is $[1\bar{1}\bar{1}]$, which is tilted 19.5° to the right with respect to $[2\bar{1}\bar{1}]$. This means that grain 1 will grow fast along $[1\bar{1}\bar{1}]$, leading to the formation of a columnar grain tilted 19.5° to the right from the coating

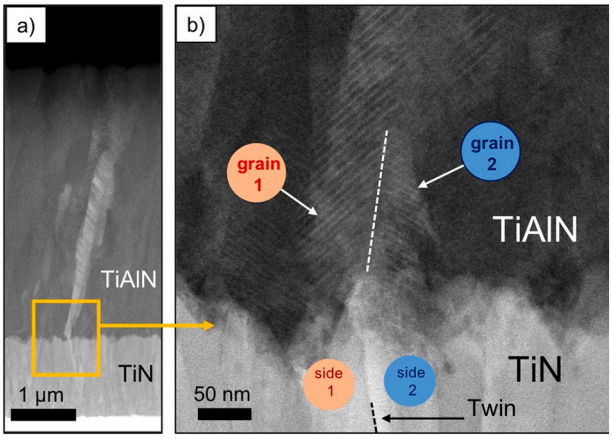

Fig. 8. a) HAADF-STEM image showing an overview of the coating consisting of columnar, inclined TiAlN grains. b) magnification of the grains marked by an arrow in Fig. 8.a highlighting the growth of two grains of TiAlN on top of a twinned grain of TiN.

normal. In a similar way, grain 2 will form a columnar grain tilted 19.5° to the left of the coating normal, which in both cases is [2$\bar{1}\bar{1}$]. As the "two-wing" model should be applied to most grains in the TiN layer, which has a ⟨211⟩ fibre texture, the TiAlN layer will also obtain a ⟨211⟩ fibre texture with {111} planes tilted 19.5° from the coating normal, as seen in Fig. 1.d. This also leads to the tilted pyramid surface morphology observed in Fig. 1.a, where the three {100} facets highlighted in Fig. 11 make up the pyramid sides.

Often a cross-section of a TiAlN coating contains grains with an uneven, "zig-zag" morphology (e.g. grain "2" in Fig. 3). This is most likely an effect of the three-dimensional nature of the coating growth. Grains are tilted some 20° from the surface normal in all different directions, not only in the plane of the cross-section (see Fig. 1d). This means that some grains cut the cross-section and are only visible over part of their length, and the boundaries between neighbouring grains can then get a serrated, zig-zag appearance. However, these grains have the same basic structure as the grains with a more regular appearance. They also have a ⟨111⟩ growth direction, {100} facets, and they contain the same nanolamella structure.

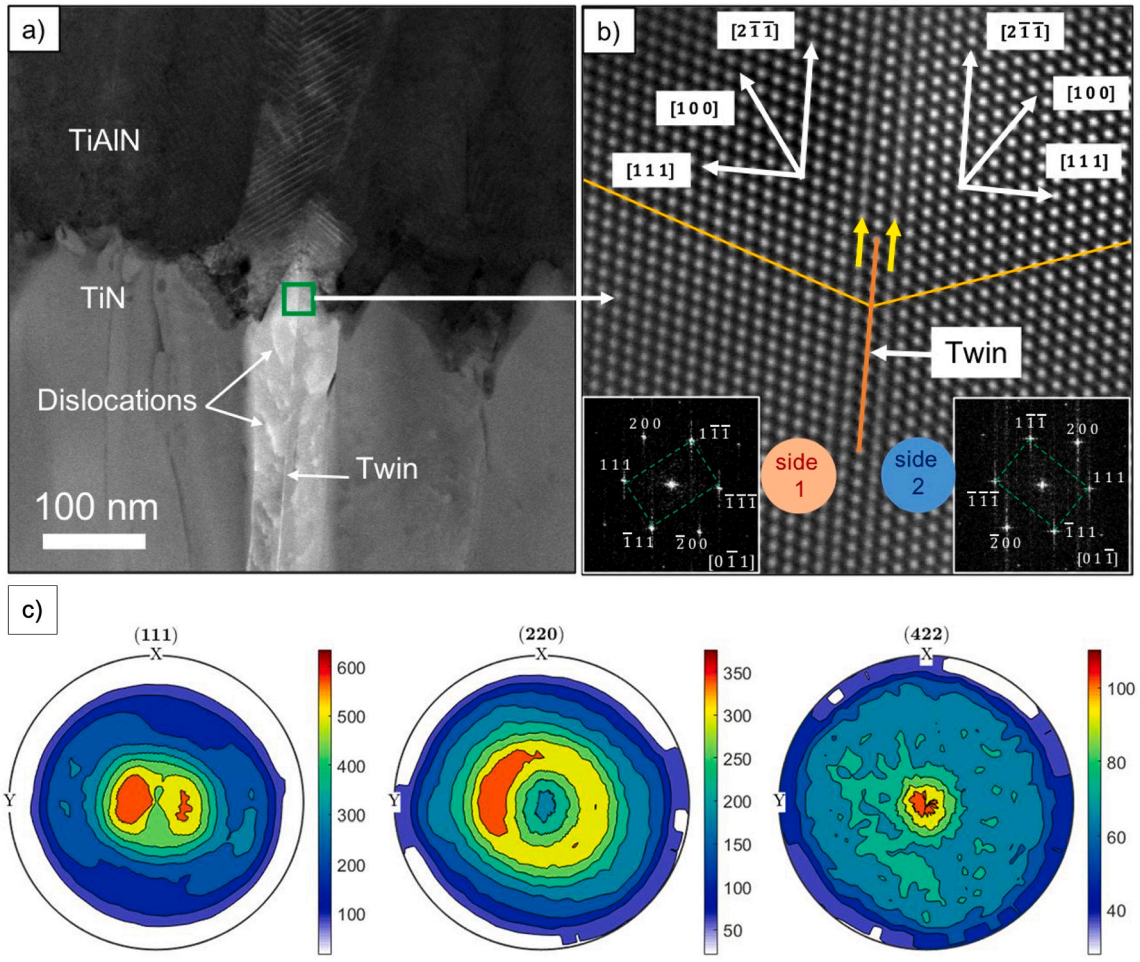

Fig. 9. a) HAADF-STEM overview of the TiN layer consisting of twinned needle-shaped grains, together with the TiAlN layer on top. Several dislocations spread in both sides of the grain (bright lines). b) Inverse FFT of a masked FFT from a HAADF-HRSTEM image, with the TiN twin plane indicated. The insets show the FFTs of each side, with a (111) twin plane. Vertical streaks are artefacts. c) XRD pole figures showing a centred intensity for (422), corresponding to a TiN ⟨211⟩ texture (along the coating normal).

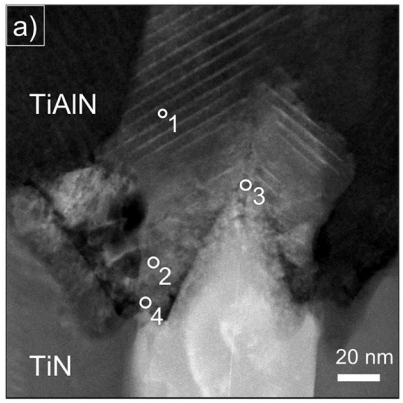

c)

(at.%)	Al	Ti	Cl
Spectrum 1´	88	12	0
Spectrum 2´	96.2	3.8	0
Spectrum 3´	70	21	9
Spectrum 4´	69.4	27	3.6

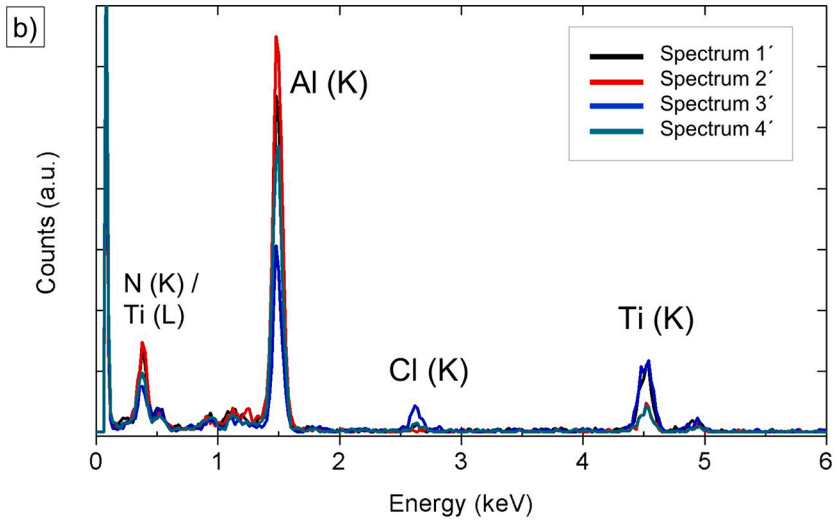

Fig. 10. a) HAADF-STEM image of the TiN/TiAlN interface. The location is the same as in Fig. 7. b) EDX spectra collected from four different points marked in Fig. 10.a. c) The table shows the concentration of Al, Ti and Cl, excluding N.

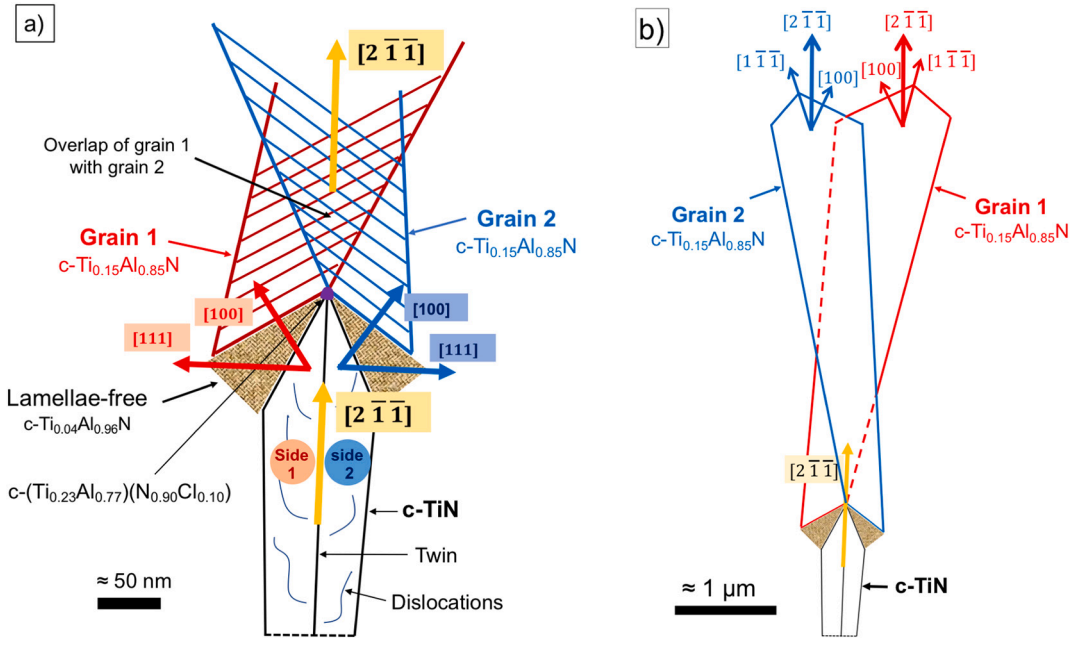

Fig. 11. Diagram of the "two-wings" growth model, highlighting the growth of two TiAlN grains on top of a twinned TiN grain. a) Interfacial and b) overview schematic drawings.

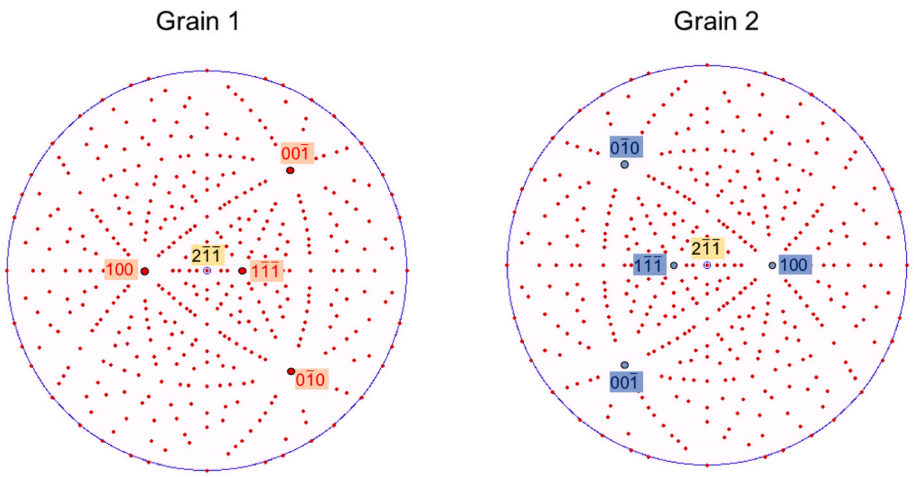

Fig. 12. Stereographic $2\bar{1}\bar{1}$ standard projections (top view, along the coating normal) for the two TiAlN grains growing on a twinned TiN grain (Fig. 11). The TiAlN grains are related by a 180° rotation along the coating normal.

5. Conclusions

- It is possible deposit ⟨211⟩-textured high Al-containing $Ti_{1-x}Al_xN$ coatings, with x-values on average around 0.85 and locally above 0.9, using LP-CVD.
- The intermediate TiN-layer with a thickness of 1.2 μm developed a ⟨211⟩ texture with twinned, V-shaped grains with needle-shaped top parts.
- The TiN-layer influenced the subsequent growth of the 4.1 μm thick TiAlN layer; both its texture and morphology.
- The TiAlN grains were columnar with a texture of ⟨211⟩, parallel to the surface normal. They grew along ⟨111⟩, with three {001} facets, leading to tilted pyramid morphology.
- The {001} facets developed an internal periodic nanolamella structure of the TiAlN grains, probably by temporal variations (rotational gas supply) of the controlling chemical reactions in combination with tendency for Ti to segregate to the surface of Al-rich lamellae. The thicknesses were 2 and 6 nm for low (x = 0.6) and high (x = 0.9) Al-containing lamellae.
- The TiAlN layer growth could be described by the "two-wing" model, where two twin-related TiAlN grains grow on a twinned TiN grain. Due to local high growth rates along ⟨111⟩, the two TiAlN grains switch sides relative to the underlying TiN grain in the coating, making the appearance of two wings, consisting of two columnar grains growing at 19.5° from the coating normal.
- In general, this work shows that it should be possible to control the growth of a TiAlN layer by controlling the texture and morphology of an intermediate TiN-layer. Of course, the growth is also influenced by the CVD process parameters.

CRediT authorship contribution statement

Mohamed Ben Hassine: Conceptualization, Methodology, Formal analysis, Investigation, Writing – original draft, Writing – review & editing. **Hans-Olof Andrén:** Supervision, Formal analysis, Writing – review & editing. **Anand H.S. Iyer:** Formal analysis, Writing – review & editing. **Antiope Lotsari:** Formal analysis, Writing – review & editing. **Olof Bäcke:** Investigation, Formal analysis, Writing – review & editing. **Dirk Stiens:** Conceptualization, Investigation, Formal analysis, Resources, Writing – review & editing. **Wiebke Janssen:** Investigation, Formal analysis, Writing – review & editing. **Thorsten Manns:** Investigation, Formal analysis, Writing – review & editing. **Johannes Kümmel:** Investigation, Formal analysis, Writing – review & editing. **Mats Halvarsson:** Conceptualization, Investigation, Formal analysis, Writing – review & editing, Supervision.

Declaration of competing interest

The authors declare that they have no known competing financial interests or personal relationships that could have appeared to influence the work reported in this paper.

Acknowledgments

This work is part of the CVD 2.0 project, supported by the Swedish Foundation for Strategic Research (SSF). This research was mainly carried out in the Chalmers Materials Analysis Laboratory (CMAL).

References

[1] W. Lengauer, K. Dreyer, Functionally graded hardmetals, J. Alloys Compd. 338 (2002) 194–212, https://doi.org/10.1016/S0925-8388(02)00232-3.
[2] H.G. Prengel, W.R. Pfouts, A.T. Santhanam, State of the art in hard coatings for carbide cutting tools, Surf. Coat. Technol. 102 (1998) 183–190, https://doi.org/10.1016/S0257-8972(96)03061-7.
[3] S. PalDey, S. Deevi, Single layer and multilayer wear resistant coatings of (Ti,Al)N: a review, Mater. Sci. Eng. A 342 (2003) 58–79, https://doi.org/10.1016/S0921-5093(02)00259-9.
[4] A. Höling, L. Hultman, M. Odén, J. Sjölén, L. Karlsson, Mechanical properties and machining performance of $Ti_{1-x}Al_xN$-coated cutting tools, Surf. Coat. Technol. 191 (2005) 384–392, https://doi.org/10.1016/j.surfcoat.2004.04.056.
[5] P.H. Mayrhofer, A. Hörling, L. Karlsson, J. Sjölén, T. Larsson, C. Mitterer, L. Hultman, Self-organized nanostructures in the Ti–Al–N system, Appl. Phys. Lett. 83 (2003) 2049–2051, https://doi.org/10.1063/1.1608464.
[6] I. Endler, M. Höhn, M. Herrmann, R. Pitonak, S. Ruppi, M. Schneider, H. van den Berg, H. Westphal, Novel aluminum-rich $Ti_{1-x}Al_xN$ coatings by LPCVD, Surf. Coat. Technol. 203 (2008) 530–533, https://doi.org/10.1016/j.surfcoat.2008.04.098.
[7] A. Paseuth, K. Yamagata, A. Miura, M. Higuchi, K. Tadanaga, Deposition and analysis of Al-rich c-$Al_xTi_{1-x}N$ coating with preferred orientation, J. Am. Ceram. Soc. 100 (2017) 343–353, https://doi.org/10.1111/jace.14549.
[8] S. Ruppi, Enhanced performance of α-Al_2O_3 coatings by control of crystal orientation, Surf. Coat. Technol. 202 (2008) 4257–4269, https://doi.org/10.1016/j.surfcoat.2008.03.021.
[9] J. Zalesak, D. Holec, I. Matko, M. Petrenec, B. Sartory, N. Koutná, R. Daniel, R. Pitonak, J. Keckes, Peculiarity of self-assembled cubic nanolamellae in the TiN/AlN system: epitaxial self-stabilization by element deficiency/excess, Acta Mater. 131 (2017) 391–399, https://doi.org/10.1016/j.actamat.2017.04.009.
[10] M. Meindlhumer, J. Zalesak, R. Pitonak, J. Todt, B. Sartory, M. Burghammer, A. Stark, N. Schell, R. Daniel, J.F. Keckes, M. Lessiak, A. Köpf, R. Weißenbacher, J. Keckes, Biomimetic hard and tough nanoceramic Ti-Al-N film with self-assembled six-level hierarchy, Nanoscale. 11 (2019) 7986–7995, https://doi.org/10.1039/c8nr10339a.
[11] J. Todt, J. Zalesak, R. Daniel, R. Pitonak, A. Köpf, R. Weißenbacher, B. Sartory, C. Mitterer, J. Keckes, Al-rich cubic $Al_{0.8}Ti_{0.2}N$ coating with self-organized nanolamellar microstructure: thermal and mechanical properties, Surf. Coat. Technol. 291 (2016) 89–93, https://doi.org/10.1016/j.surfcoat.2016.02.027.
[12] J. Zalesak, J. Todt, R. Pitonak, A. Köpf, R. Weißenbacher, B. Sartory, M. Burghammer, R. Daniel, J. Keckes, Combinatorial refinement of thin-film microstructure, properties and process conditions: iterative nanoscale search for self-assembled TiAlN nanolamellae, J. Appl. Crystallogr. 49 (2016) 2217–2225, https://doi.org/10.1107/S1600576716017258.

[13] R. Qiu, A. Forslund, O. Bäcke, A.H.S. Iyer, M. Sattari, W. Janssen, T. Manns, J. Kümmel, A. Ruban, D. Stiens, H.O. Andrén, M. Halvarsson, Effects of gas flow on detailed microstructure inhomogeneities in LPCVD TiAlN nanolamella coatings, Materialia. 9 (2020), 100546, https://doi.org/10.1016/j.mtla.2019.100546.
[14] R. Qiu, O. Bäcke, D. Stiens, W. Janssen, J. Kümmel, T. Manns, H.O. Andrén, M. Halvarsson, CVD TiAlN coatings with tunable nanolamella architectures, Surf. Coat. Technol. 413 (2021), 127076, https://doi.org/10.1016/j.surfcoat.2021.127076.
[15] H.E. Cheng, M.H. Hon, Texture formation in titanium nitride films prepared by chemical vapor deposition, J. Appl. Phys. 79 (1996) 8047–8053, https://doi.org/10.1063/1.362358.
[16] Powder Diffraction File, Card 00-046-1200, International Center for Diffraction Data, n.d.
[17] A. Madan, I.W. Kim, S.C. Cheng, P. Yashar, V.P. Dravid, S.A. Barnett, Stabilization of cubic AlN in epitaxial AlN/TiN superlattices, Phys. Rev. Lett. 78 (1997) 1743–1746, https://doi.org/10.1103/PhysRevLett.78.1743.
[18] P.E. Batson, N. Dellby, O.L. Krivanek, Sub-Ångstrom resolution using aberration corrected electron optics, Nature. 418 (2002) 617–620, https://doi.org/10.1038/nature00972.
[19] P.D. Nellist, M.F. Chisholm, N. Dellby, O.L. Krivanek, M.F. Murfitt, Z.S. Szilagyi, A. R. Lupini, A. Borisevich, W.H. Sides, S.J. Pennycook, Direct sub-angstrom imaging of a crystal lattice, Science. 305 (2004) 1741, https://doi.org/10.2116/science.1100965.
[20] S. Van Aert, J. Verbeeck, R. Erni, S. Bals, M. Luysberg, D. Van Dyck, G. Van Tendeloo, Quantitative atomic resolution mapping using high-angle annular dark field scanning transmission electron microscopy, Ultramicroscopy. 109 (2009) 1236–1244, https://doi.org/10.1016/j.ultramic.2009.05.010.
[21] T. Grieb, K. Müller, R. Fritz, V. Grillo, M. Schowalter, K. Volz, A. Rosenauer, Quantitative chemical evaluation of dilute GaNAs using ADF STEM: avoiding surface strain induced artifacts, Ultramicroscopy. 129 (2013) 1–9, https://doi.org/10.1016/j.ultramic.2013.02.006.
[22] S.J. Pennycook, Z-contrast stem for materials science, Ultramicroscopy. 30 (1989) 58–69, https://doi.org/10.1016/0304-3991(89)90173-3.
[23] E.M. James, N.D. Browning, Practical aspects of atomic resolution imaging and analysis in STEM, in: Ultramicroscopy, Elsevier Science Publishers B.V., 1999, pp. 125–139, https://doi.org/10.1016/S0304-3991(99)00018-2.
[24] J.I. Goldstein, J.L. Costley, G. Lorimer, S.J.B. Reed, in: O. Johari (Ed.), Quantitative X-ray Microanalysis in the Electron Microscope SEM 1977 1, IITRI, Chicago IL, 1977, pp. 315–325, n.d.
[25] Z. Yu, D.A. Muller, J. Silcox, Study of strain fields at a-Si/c-Si interface, J. Appl. Phys. 95 (2004) 3362–3371, https://doi.org/10.1063/1.1649463.
[26] H.E. Cheng, Y.W. Wen, Correlation between process parameters, microstructure and hardness of titanium nitride films by chemical vapor deposition, Surf. Coat. Technol. 179 (2004) 103–109, https://doi.org/10.1016/S0257-8972(03)00789-8.
[27] A. Forslund, A. Ruban, Surface energetics of $Al_xTi_{1-x}N$ alloys, Comput, Mater. Sci. 183 (2020), 109813, https://doi.org/10.1016/j.commatsci.2020.109813.